Spin-Torque Ferromagnetic Resonance in W/Co-Fe-B/W/Co-Fe-B/MgO Stacks

Congli He,[1,2,3] Guoqiang Yu,[2,*] Cecile Grezes,[3] Jiafeng Feng,[2] Zhen Zhao,[3,4] Seyed Armin Razavi,[3] Qiming Shao,[3] Aryan Navabi,[3] Xiang Li,[3] Qing Lin He,[3] Mengyin Li,[5] Jia Zhang,[5] Kin L. Wong,[3] Dan Wei,[4] Guangyu Zhang,[2] Xiufeng Han,[2,†] Pedram Khalili Amiri,[3] and Kang L. Wang[3,6,7,‡]

[1]*Institute of Advanced Materials, Beijing Normal University, Beijing 100875, China*
[2]*Beijing National Laboratory for Condensed Matter Physics, Institute of Physics, Chinese Academy of Sciences, Beijing 100190, China*
[3]*Department of Electrical and Computer Engineering, University of California, Los Angeles, California 90095, USA*
[4]*Key Laboratory of Advanced Materials (MOE), School of Materials Science and Engineering, Tsinghua University, Beijing 100084, China*
[5]*School of Physics and Wuhan National High Magnetic Field Center, Huazhong University of Science and Technology, 430074 Wuhan, China*
[6]*Department of Physics & Astronomy, University of California, Los Angeles, California 90095, USA*
[7]*Department of Materials Science Engineering, University of California, Los Angeles, California 90095, USA*

(Received 28 September 2017; revised manuscript received 30 May 2018; published 28 September 2018)

We investigate the magnetic properties of as-grown and annealed W/Co-Fe-B/W(insertion)/Co-Fe-B/MgO stacks with different thicknesses of Co-Fe-B layers and W insertion layers using spin-torque ferromagnetic resonance (ST FMR) technique. The dependences of perpendicular magnetic anisotropy (PMA), damping constant, and interlayer exchange coupling on the annealing, Co-Fe-B layer thicknesses, and W insertion layer thicknesses are systematically studied. The PMA is strongly enhanced after annealing at 400 °C. Nevertheless, the Gilbert damping constant remains nearly unchanged after annealing. The PMA also increases with the thickness of the W insertion layer. Both acoustic (in-phase) mode and optical (out-of-phase) mode are observed. The optical mode, which is typically weak when using the conventional FMR measurement, shows a comparable magnitude to the acoustic mode. The effective excitation of the optical mode is ascribed to the nonuniform spin-orbit torque acting on the two coupled layers. Furthermore, the interlayer exchange coupling (ferromagnetic or antiferromagnetic) can be identified through analyzing the two resonance modes, which is found to depend on the W insertion layer thickness, Co-Fe-B layer thickness, and annealing conditions. The experimental results will be useful for developing high-frequency magnetic devices based on magnetic multilayer films with high PMA and thermal stability. Our experimental results also show that the ST FMR is an effective methodology for studying interlayer exchange coupled systems.

DOI: 10.1103/PhysRevApplied.10.034067

I. INTRODUCTION

Magnetic tunnel junctions (MTJs) with a perpendicular magnetic anisotropy (PMA) have attracted tremendous attention for their potential in developing high density, high thermal stability, and low-power consumption spin-transfer-torque (STT)/spin-orbit-torque (SOT) magnetic random access memory (MRAM) [1–6]. Among the available PMA systems that are compatible with MTJs, the heavy metal/Co-Fe-B/MgO system has demonstrated the capability of facilitating a high tunneling magnetoresistance (TMR) ratio and compatibility with complementary metal-oxide-semiconductor (CMOS) technology [3,7,8]. Moreover, this structure allows SOT-driven magnetization switching, offering advantages over conventional STT in terms of power consumption and the fact that the high write current does not pass through the tunnel barrier of the MTJ [3,9].

To increase data retention time, a strong PMA is required. In the heavy metal/Co-Fe-B/MgO films, the PMA mainly originates from the interfacial PMA at the Co-Fe-B/MgO interface [3]. Nevertheless, the heavy metal/Co-Fe-B interface also plays an important role in achieving high PMA [10]. It has been found that the PMA can be increased by inserting ultrathin metals in the Co-Fe-B layer [11–16]. Very recently, a high PMA has been reported in the MgO/Co-Fe-B/W(insertion)/Co-Fe-B/W (from bottom

*guoqiangyu@iphy.ac.cn
†xfhan@iphy.ac.cn
‡wang@ee.ucla.edu

to top) and MgO/Co-Fe-B/W(insertion)/Co-Fe-B/MgO stacks [17,18], which also show high thermal stability, making them more promising for practical applications. The former structure is of particular interest because the top W layer with a large spin Hall angle allows energy-efficient manipulation of the perpendicular magnetization using in-plane current-induced SOTs [4,19]. However, it is still unclear how the thicknesses of the Co-Fe-B and W insertion layers affect the PMA as well as other magnetic characteristics, such as the resonance frequency and field, Gilbert damping constant (α), and interlayer coupling modes. Understanding all of these properties can help improve the contribution/role of the materials toward practical applications.

In this work, we study the ferromagnetic resonance properties of the W/Co-Fe-B/W(insertion)/Co-Fe-B/MgO (from bottom to top) structures using the spin-torque ferromagnetic resonance (ST FMR) technique [20–22]. The thicknesses of Co-Fe-B and W insertion layers are systematically adjusted to explore their effects on the PMA. More importantly, the influence of annealing, Co-Fe-B layer thickness, and W insertion layer thickness on the magnetic damping constants and interlayer exchange coupling can be identified by analyzing the ST FMR spectra. These results may be useful for developing high-frequency magnetic devices based on magnetic multilayer films with high PMA and thermal stability.

II. SAMPLE PREPARATION AND ST FMR MEASUREMENT

The stacks consisting of W(5)/Co-Fe-B(t_1)/W(t)/Co-Fe-B(t_2)/MgO(2)/Ta(2) ($t_1 = t_2$, thicknesses are in nm) are deposited on thermally oxidized Si(001) substrates by a magnetron sputtering system at room temperature. The two Co-Fe-B layers are grown in a wedge shape with the thicknesses varying from 0.69 to 1.31 nm, as shown in Fig. 1(a). Subsequently, the multilayer stacks are patterned into rectangular-shaped strips (length of 20 μm and width of 20 μm) using optical lithography and dry etching. Cr(10)/Au(100) metal stacks are deposited as electrodes for electrical measurements. The annealing treatment is carried out at 400 °C for 0.5 h in a vacuum environment without an external magnetic field. Figure 1(b) shows the schematic diagram of the ST FMR measurement setup. A microwave current $I_{c,\mathrm{rf}}$ with a power of 6 dBm is applied to the device to generate a microwave-frequency SOT on the ferromagnetic layers, which oscillates the magnetization, resulting in an oscillation of the longitudinal resistance due to spin hall magnetoresistance (SMR) effect. A rectified voltage V_{mix} due to the mixing of rf current and the time-varying resistance is detected by using a lock-in amplifier. An in-plane magnetic field with a fixed angle θ_H of 45° is swept between −0.5 and +0.5 T, where θ_H is the angle between the external field and the current channel. All the measurements are carried out at room temperature.

III. EXPERIMENTAL RESULTS AND DISCUSSION

A. ST FMR spectra of the magnetic multilayer stacks

Figure 1(c) shows the typical ST FMR spectra for the as-grown sample with Co-Fe-B layers of $t_1 + t_2 = 1.95$ nm and a W insertion layer of 0.4 nm. The spectrum can be well fitted to the sum of symmetric and antisymmetric

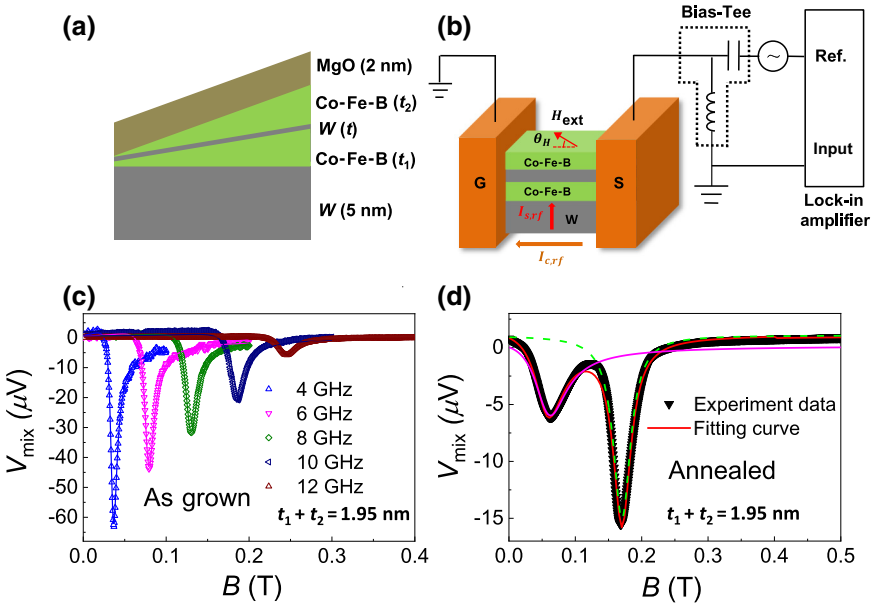

FIG. 1. (a) The schematic diagram of the magnetic multilayer stack with a W insertion layer. (b) The schematic diagram of the ST FMR measurement setup. The charge current $I_{c,\mathrm{rf}}$ is marked by the orange arrow, and the spin current $I_{s,\mathrm{rf}}$ is indicated by the red arrow. H_{ext} is the applied external magnetic field. θ_H is the angle between H_{ext} and the current channel. (c) The ST FMR spectra for the as-grown sample with Co-Fe-B layers of $t_1 + t_2 = 1.95$ nm and a W insertion layer of 0.4 nm. The solid curves are the fits to a sum of symmetric and antisymmetric Lorentzian functions. (d) The ST FMR spectrum for the annealed sample under a frequency of 3.0 GHz. The same device is measured to obtain the results before (c) and after (d) annealing. Two resonance peaks are observed, which is a signature of PMA.

Lorentzian functions [23],

$$V_{\mathrm{mix}} = S\frac{\Delta^2}{\Delta^2 + (\mu_0 H_{\mathrm{ext}} - \mu_0 H_0)^2} + A\frac{\Delta(\mu_0 H_{\mathrm{ext}} - \mu_0 H_0)}{\Delta^2 + (\mu_0 H_{\mathrm{ext}} - \mu_0 H_0)^2} \quad (1)$$

which mainly originate from the dampinglike SOT and fieldlike SOT as well as Oersted field torque, respectively [24]. Δ is the linewidth (full width at half maximum), $\mu_0 H_0$ is the resonant magnetic field, $\mu_0 H_{\mathrm{ext}}$ is the applied magnetic field, S is the symmetric Lorentzian coefficient that is proportional to the oscillating spin current $I_{s,\mathrm{rf}}$, and A is the antisymmetric Lorentzian coefficient that is proportional to the Oersted field $\mu_0 H_{\mathrm{rf}}$ generated by I_{rf}. One single resonance peak is observed for a given frequency, and the resonance magnetic field increases with the frequency, which is a typical signature resulting from the in-plane magnetic anisotropy. Figure 1(d) shows a ST FMR spectrum for the annealed sample. In contrast to the spectra for the as-grown samples [Fig. 1(c)], two resonance peaks are observed for the annealed samples, which is a signature of PMA [22]. The two peaks can be separately fitted using Eq. (1). The linewidth Δ and resonant magnetic field $\mu_0 H_0$ are thus extracted and used for analyzing the magnetic anisotropy and damping constant as discussed in the following sections.

B. The effective magnetization fields and gilbert damping

Figure 2(a) shows the resonance frequency f as a function of resonant field $\mu_0 H_0$ for as-grown samples with different Co-Fe-B thicknesses and a 0.4-nm-thick W insertion layer. The effective magnetization fields $4\pi M_{\mathrm{eff}}$ are extracted from the Kittel equation fitting [19,23,25],

$$f = (\gamma/2\pi)[\mu_0 H_0(\mu_0 H_0 + 4\pi M_{\mathrm{eff}})]^{1/2} \quad (2)$$

where γ is the gyromagnetic ratio. Figure 2(b) shows the dependences of resonance frequency f on the resonant field $\mu_0 H_0$ for the annealed samples. Compared with the results for as-grown samples, the most striking feature for the annealed samples is the emergence of an additional branch at a low-field region as the thicknesses of Co-Fe-B layers decrease (e.g., $t_1 + t_2 = 1.88$ nm). This additional branch corresponds to the additional resonance peak at a low-field region for the perpendicularly magnetized samples, as shown in Fig. 1(d). For the samples with a PMA, the magnetization is not aligned with the external magnetic field as the magnitudes of the field are below the alignment field $\mu_0 H_a^{\mathrm{FMR}}$. For the right branch, $H_0 > H_a^{\mathrm{FMR}}$, the resonant frequency dependence on the magnetic field can still be approximately fitted by the Kittel equation.

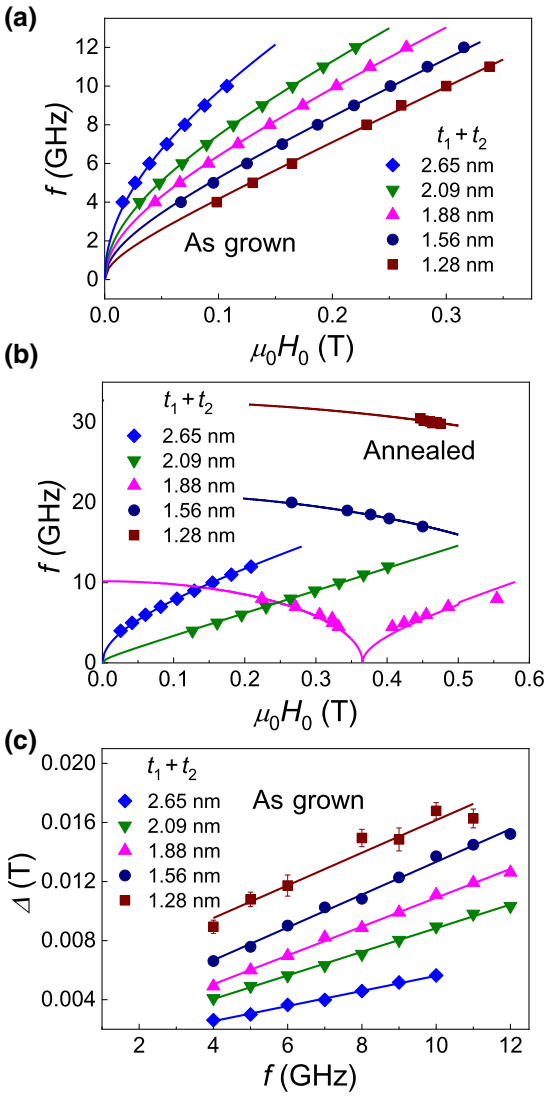

FIG. 2. Resonance frequency f as a function of the resonant field $\mu_0 H_0$ for the as-grown (a) and annealed (b) samples with different Co-Fe-B layer thicknesses. The W insertion layer thickness is 0.4 nm. The solid lines are fitting curves. For the annealed sample (e.g., $t_1 + t_2 = 1.88$ nm), the resonance frequency dependence on the resonant field exhibits an additional branch as the thickness of the Co-Fe-B stacks decrease. (c) The linewidth Δ extracted from the fitting of ST FMR spectra versus the resonance frequency f for different Co-Fe-B layer thicknesses. The lines are linear fittings.

For $H_0 < H_a^{\mathrm{FMR}}$, the left branch can be described by the following equation:

$$f = (\gamma/2\pi)[(\mu_0 H_k)^2 - (\mu_0 H_0)^2]^{1/2} \quad (0 < H_0 < H_k) \quad (3)$$

which was derived from previous work [26]. Here, $\mu_0 H_k = \mu_0 H_\perp - 4\pi M_S = -4\pi M_{\mathrm{eff}}$.

Figure 3(a) shows the extracted effective magnetization fields as a function of Co-Fe-B layer thickness for

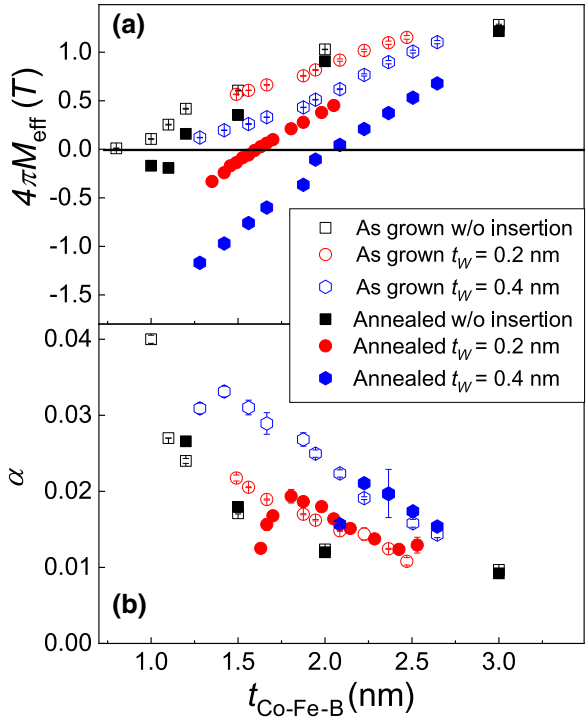

FIG. 3. (a) The effective magnetization fields, $4\pi M_{\text{eff}}$, as a function of Co-Fe-B thickness for the as-grown and annealed samples with and without (reported in Ref. [21]) W insertion layers. (b) The Gilbert damping constant α, for the as-grown and annealed samples, extracted from the linear fitting of the linewidth versus the frequency f.

the samples with W insertion layer thicknesses of 0.2 nm (red circle) and 0.4 nm (blue hexagon). The results for the sample with single layer Co-Fe-B (reported in Ref. [21]), i.e., without a W insertion layer, are also shown in the figure for comparison (black square). The values of $4\pi M_{\text{eff}}$ are positive for all the as-grown samples, implying an in-plane magnetic anisotropy. For a given Co-Fe-B layer thickness, $4\pi M_{\text{eff}}$ decreases after inserting a W layer, reflecting the enhancement of PMA. Since the PMA also originates from the interface between Co-Fe-B and heavy metal, such an enhancement is ascribed to the additional Co-Fe-B/W interfaces [10,17,18]. Furthermore, compared with the PMA for the sample with a 0.2-nm-thick W insertion layer, the enhancement for the 0.4 nm case is more pronounced. This again reflects the importance of high-quality interfaces because the 0.4-nm-thick W insertion layer has better continuity and uniformity compared to the 0.2-nm-thick one. After annealing the samples, $4\pi M_{\text{eff}}$ becomes negative for the samples with relatively thin Co-Fe-B layers, indicating that the anisotropy field of the system changes from in-plane to out-of-plane. The samples with W insertion layers have a more pronounced increase of PMA compared with those without W insertion, again indicating that the W/Co-Fe-B interface helps to enhance the PMA [10].

The frequency dependences of resonance linewidths are summarized in Fig. 2(c). The resonance linewidth can be fitted by [19,25]:

$$\Delta = \Delta_0 + (2\pi\alpha/\gamma)f \tag{4}$$

where Δ_0 is the extrinsic contribution (e.g., inhomogeneous broadening) to the linewidth, which is usually independent of frequency. The second term is the intrinsic contribution (e.g., Gilbert damping), which is linearly proportional to frequency. The α values for the samples with 0.2- and 0.4-nm-thick W insertion layers as a function of Co-Fe-B thickness are then extracted and shown in Fig. 3(b). The as-grown and annealed samples with 0.2-nm-thick W insertion layers show comparable α values and similar dependences on the Co-Fe-B layer thickness to the sample without an insertion layer. Increasing the W insertion layer thickness leads to the increase of α for a given Co-Fe-B thickness. We also notice that different from the as-grown samples, α does not increase monotonously as the thickness of Co-Fe-B stacks decreases in the annealed samples with the W insertion layer. Instead, α first increases along with the decrease of the Co-Fe-B thickness, but then decreases abruptly at some critical Co-Fe-B thickness. This may be related to the increased interfacial PMA, which requires further investigation.

C. The exchange coupling between the Co-Fe-B layers

Figures 4(a) and 4(b) show the ST FMR spectra (13 GHz) for the as-grown and annealed samples with Co-Fe-B layer thicknesses of $t_1 + t_2 = 2.37$ nm and a 0.6-nm-thick W insertion layer. Strikingly, two peaks are observed in ST FMR spectra for both as-grown and annealed samples of $t_1 + t_2 > 2.0$ nm, as shown by the green and blue fitting curves. Notably, the linewidth of the green one is much narrower than that of the blue one for both the as-grown and annealed samples, as shown in Figs. 4(c) and 4(d). Interestingly, the resonance field of the narrower linewidth is lower than that of the wider one for the as-grown sample, as shown in Fig. 4(a), while the resonance field of the narrower one becomes larger than that of the wider one after annealing, as shown in Fig. 4(b). Such a feature is visible for all the measured frequency range, as shown in Figs. 4(e) and 4(f). We point out that these two peaks have different origins compared to those of the samples with PMA. First of all, the dependence of resonant frequency on the resonant field for both the narrower and wider peaks follows the Kittel equation, indicating that the film exhibits an in-plane magnetic anisotropy. The in-plane magnetic anisotropy is further verified by the extracted positive values of $4\pi M_{\text{eff}}$ for the as-grown and annealed

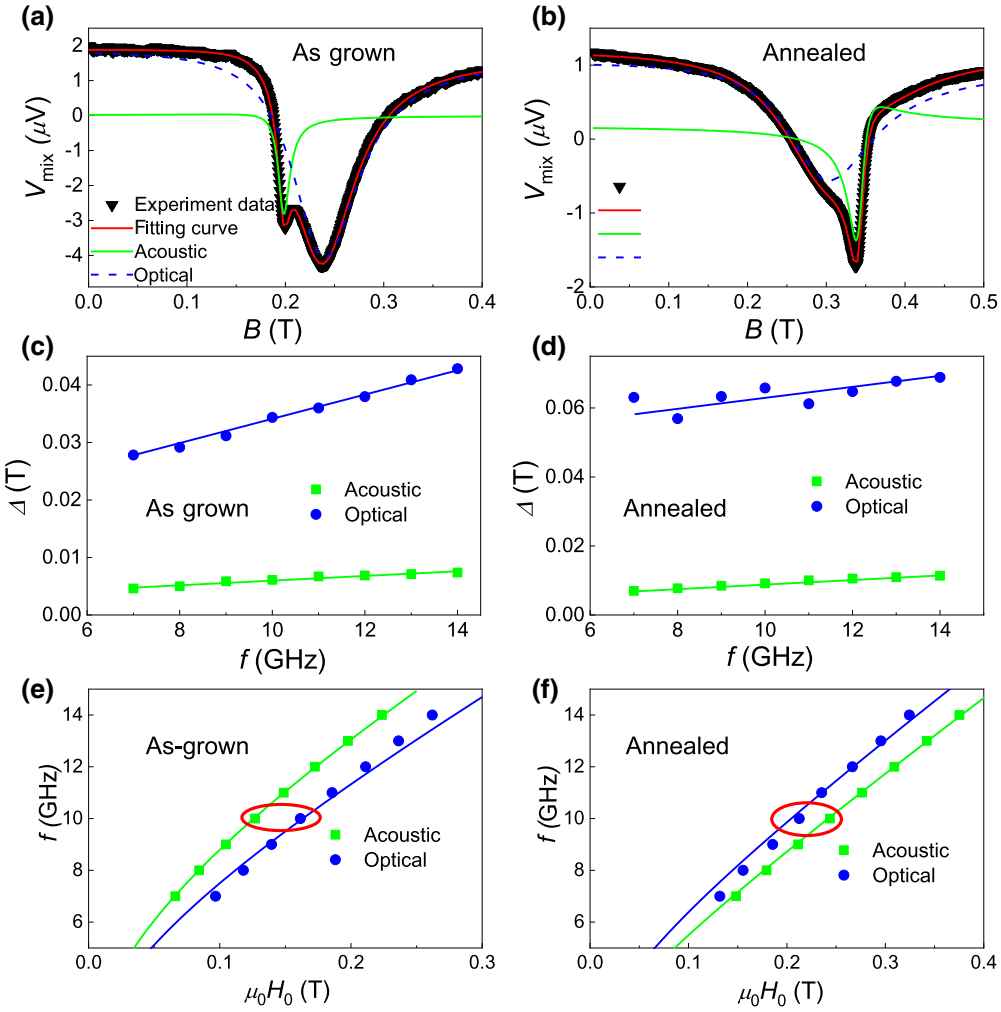

FIG. 4. The ST FMR spectra (13 GHz) for the as-grown (a) and annealed (b) samples with Co-Fe-B layer thicknesses of $t_1 + t_2 = 2.37$ nm and a 0.6-nm-thick W insertion layer. Two peaks are observed in both ST FMR spectra, which are attributed to the symmetric (acoustic) and antisymmetric (optical) modes. The fitting curves are indicated by the lines. The linewidth Δ as a function of the resonance frequency f for the as-grown (c) and annealed (d) samples. Resonance frequency f as a function of the resonant field $\mu_0 H_0$ for the two different modes, in as-grown (e) and annealed (f) samples. The solid curves are fittings by Kittel equation.

samples [see Fig. 5(a)] and by magneto-optical Kerr effect (MOKE) measurement (to be discussed later).

We attribute the observation of two resonance peaks to the emergence of two different modes of the ferromagnetic resonance of the Co-Fe-B/W/Co-Fe-B layers. In addition to the in-phase resonance, the weak coupling between the two Co-Fe-B layers can also lead to an out-of-phase resonance. These two modes had been previously observed in NiFe/Ru/NiFe and Fe/$[Co/Cu]_{10}$/Co/Pt structures [27–30]. The in-phase and out-of-phase resonances are referred to as the acoustic (symmetric) mode and the optical (antisymmetric) mode, respectively. Another pronounced feature observed in the previous experiments is that the linewidths (as well as the Gilbert damping) of the optical modes are greater than those of the acoustic modes [27,28,31], which are consistently shown by our results [see Fig. 5(b)]. The damping constants of the acoustic modes remain relatively low, while those of the optical modes increase (for $t_1 + t_2 > 2.0$ nm). This can be qualitatively explained by the framework of the mutual spin pumping effect [27,31]. In the out-of-phase precession, the pumped spin accumulation and spin current are greatly amplified compared to those of the in-phase precession mode, resulting in a giant enhancement of the Gilbert damping in the out-of-phase precession mode [27,29,31].

The resonance fields of the acoustic ($\mu_0 H_0^S$) and optical ($\mu_0 H_0^A$) modes can be described by [29]:

$$\mu_0 H_0^A = \mu_0 H_0^S + 2\mu_0 H_{ex} \quad \mu_0 H_{ex} = -A_{ex}/M_S t_F \qquad (5)$$

where A_{ex} is the strength of the exchange coupling and t_F is the thickness of the ferromagnetic layer ($t_F = t_1 = t_2$). A positive A_{ex} corresponds to ferromagnetic (FM) coupling and a negative one corresponds to antiferromagnetic (AFM) coupling [28]. Therefore, the optical mode has the lower resonance field in the FM-coupled system, while it has a higher resonance field in the AFM-coupled system. We are able to extract the coupling fields $\mu_0 H_{ex}$ by directly measuring the difference between the acoustic and optical mode resonance fields, as shown in Fig. 6(a). The exchange coupling strengths A_{ex} are, therefore, extracted through Eq. (5) using $M_s = 1.008$ MA/m as reported by

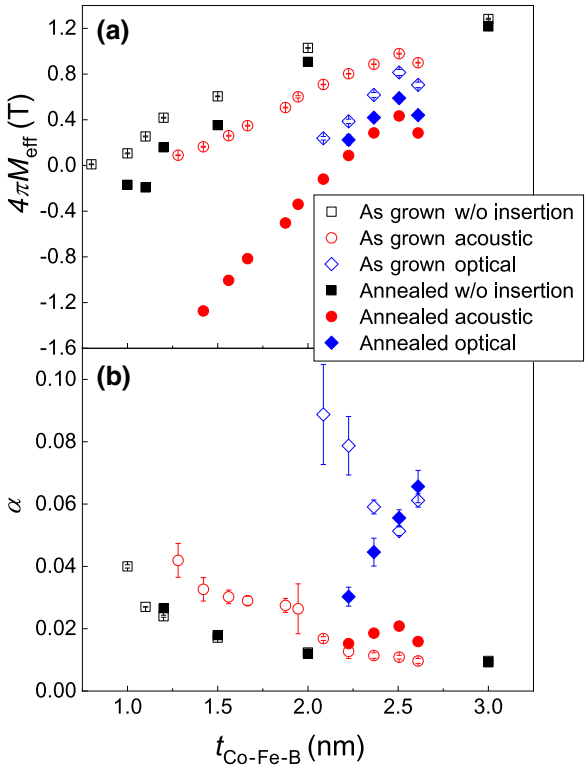

FIG. 5. (a) The effective magnetization fields ($4\pi M_{eff}$) and (b) the Gilbert damping constant α for the as-grown and annealed samples with and without a W insertion layer as a function of Co-Fe-B thickness. The W insertion layer thickness is 0.6 nm.

our previous work [22]. A_{ex} is negative for the as-grown samples, indicating an AFM coupling between the two Co-Fe-B layers. However, for the annealed sample, A_{ex} is positive, indicating an FM coupling between the two Co-Fe-B layers. We point out that, for $t_1 + t_2 < 2.0$ nm, only one resonance peak is observed. This implies that the two Co-Fe-B layers are strongly coupled with each other, similar to a single layer of Co-Fe-B. These results indicate that the coupling between the two Co-Fe-B layers is not only dependent on the W insertion layer thickness, but also on the Co-Fe-B layer thickness.

To further verify the obtained coupling types in as-grown and annealed samples, magnetic hysteresis loops are measured by MOKE, as shown in Fig. 6(b). In the upper panel, the hysteresis loop of the as-grown sample with $t_1 + t_2 = 2.55$ nm shows an AFM coupling [16,32,33]. However, after annealing, this sample changes to show FM coupling (the middle panel). In the lower panel, the hysteresis loop of the as-grown sample with Co-Fe-B layer thickness of $t_1 + t_2 = 1.56$ nm shows an FM exchange coupling. The results of the MOKE measurements confirm our inference from ST FMR spectra analysis.

It is known that two ferromagnetic layers that are separated by a nonmagnetic metal can be indirectly coupled

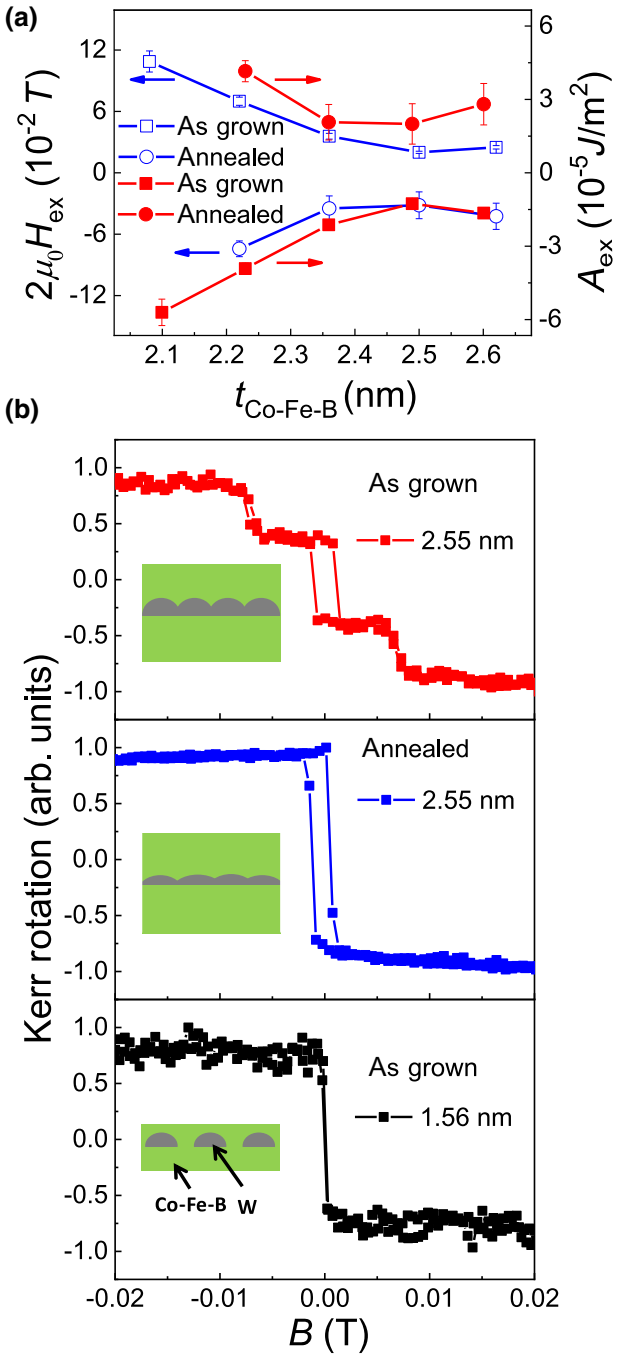

FIG. 6. (a) The interlayer exchange coupling extracted from the resonance field shift of the acoustic and optical modes ($t_{CoFeB} = t_1 + t_2$). A_{ex} is negative for the as-grown samples, corresponding to an antiferromagnetic coupling. However, for the annealed samples, A_{ex} becomes positive, corresponding to a ferromagnetic coupling. (b) In-plane magnetic hysteresis loops for the as-grown and annealed Co-Fe-B stacks. The upper panel: The hysteresis loop shows antiferromagnetic coupling (as-grown, $t_1 + t_2 = 2.55$ nm). The middle panel: The hysteresis loop shows ferromagnetic coupling (annealed, $t_1 + t_2 = 2.55$ nm). The lower panel: The hysteresis loop shows ferromagnetic exchange coupling (as-grown, $t_1 + t_2 = 1.56$ nm). The insets are the corresponding Co-Fe-B/W/Co-Fe-B film structures.

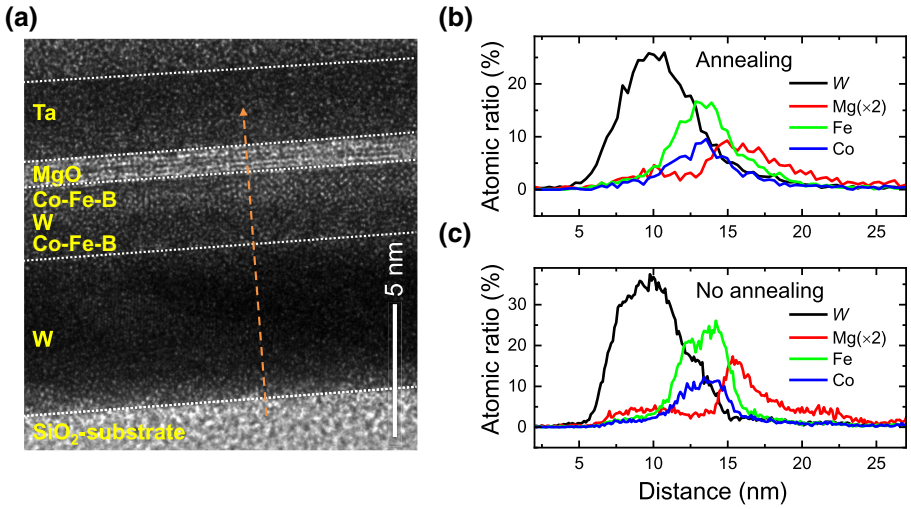

FIG. 7. (a). The high-resolution TEM image of as-grown W(5)/Co-Fe-B (1.28)/W(0.6)/Co-Fe-B(1.28)/MgO(2) /Ta(2) (units in nm), (b),(c) the line profiles [along the orange dashed line direction in (a)] for individual elements extracted from the high-angle annular dark-field images with line scan-energy dispersive spectra for the annealed and nonannealed samples, respectively.

through the Ruderman-Kittel-Kasuya-Yosida (RKKY) interaction [34–36]. The coupling can be either ferromagnetic or antiferromagnetic, depending on the sign of the coupling coefficient J_{ij}^{RKKY}, which shows an oscillatory behavior as a function of the thickness of the spacer layer [35–38]. For the samples with an insertion layer of 0.6 nm, the two Co-Fe-B layers with $t_1 + t_2 > 2.0$ nm are likely coupled through indirect RKKY interaction in an antiferromagnetic manner. After annealing, the exchange coupling in the sample with a 0.6-nm-thick W insertion layer changes from AFM to FM correspondingly, as shown in the upper and middle panels of Fig. 6(b). We believe this transition is related to the interdiffusion among the layers promoted by the annealing process, which is revealed by the transmission electron microscopy measurement. Figure 7(a) shows the samples structure of the studied sample. The interdiffusion between W and Co-Fe-B layers can be proved by the line profiles for individual elements as shown in Figs. 7(b) and 7(c), which are extracted from the high-angle annular dark-field images with line scan-energy dispersive spectra. We speculate that the interdiffusion changes the effective W layer thickness, which changes the coupling coefficient J_{ij}^{RKKY}. It is noted that the orange-peel coupling can also result in parallel or antiparallel interlayer coupling for perpendicular magnetization due to the relatively large surface roughness (approximately 12 Å) [39]. In our multilayers, the surface roughness is <5 Å based on a TEM image, and thus, we speculate that the orange-peel coupling plays a minor role.

It is counterintuitive to conclude that the coupling type varies with the Co-Fe-B layer thickness. This may imply that the morphology of the insertion layer also depends on the Co-Fe-B thickness. For the samples with Co-Fe-B stacks thinner than 2.0 nm, the surface morphology may not allow for the growth of a continuous W layer, as shown in the inset of the lower panel of Fig. 6(b). Similar to this situation, for the samples with 0.2- and 0.4-nm-thick W insertion layers, the W insertion layer may be too thin to be continuous as well. As a result, the Co-Fe-B layers cannot be well separated, resulting in a direct exchange coupling.

Our results indicate that the ST FMR can be used to excite and identify the acoustic and optical resonance modes of interlayer exchange-coupled ferromagnetic layers, which are typically accomplished by FMR technique. In addition to providing an alternative technique, there is an extra advantage in using ST FMR. For a conventional FMR technique, the signal magnitude of the excited optical mode is typically much smaller than the acoustic mode because the out-of-phase resonance cannot efficiently couple to a uniform excitation magnetic field over the sample [30,40], especially for two identical ferromagnetic layers. This problem can be overcome via using a ST FMR technique. Different from the uniform magnetic field excitation, the SOT is not uniformly applied to the two ferromagnetic layers. In the studied sample, the SOT is mainly applied to the Co-Fe-B layer that is adjacent to the bottom W layer. This is because the spin current generated from the W layer is mainly absorbed by the adjacent Co-Fe-B layer and barely diffuses into the second Co-Fe-B layer. As a result, the excitation of the optical mode is more efficient and the magnitude is pronounced in our experiment.

IV. CONCLUSION

We investigate the magnetic properties of both the as-grown and annealed W/Co-Fe-B/W/Co-Fe-B/MgO stacks with different thicknesses of the Co-Fe-B and W insertion layers using ST FMR technique. By analyzing the ST FMR spectra, we systematically study the dependences of the magnetic anisotropy, damping constant, and interlayer exchange coupling on the effects of annealing, Co-Fe-B layer thicknesses, and W insertion layer thicknesses. It is found that the PMA is strongly enhanced after annealing, while the Gilbert damping constant remains nearly unchanged. The PMA also increases with increasing

the thickness of the W insertion layer. The direct exchange coupling or indirect RKKY interaction between the two Co-Fe-B layers can also be identified using ST FMR technique, which is found to depend on the W insertion layer thickness, Co-Fe-B layer thickness, and annealing conditions. Our results indicate that the ST FMR measurement is also an effective methodology for probing the interlayer exchange coupling between magnetic multilayers. Our present work will be useful for designing and developing magnetic devices using W-based structures with large PMA and high thermal stability.

ACKNOWLEDGMENTS

This work was supported by financial support from the National Natural Science Foundation of China (NSFC, Grant No.11874409), National Natural Science Foundation of China (NSFC)-Science Foundation Ireland (SFI) Partnership Programme (Grant No. 51861135104), and 1000 Youth Talents Program. This work was also supported in part by C-SPIN and FAME, two of six centers of STARnet, a Semiconductor Research Corporation program, sponsored by MARCO and DARPA. This work was also supported by the National Science Foundation (Grant No. ECCS 1611570) and Nanosystems Engineering Research Center for Translational Applications of Nanoscale Multiferroic Systems (TANMS) Cooperative Agreement Award No. EEC-1160504.

[1] S. Mangin, D. Ravelosona, J. A. Katine, M. J. Carey, B. D. Terris, and E. E. Fullerton, Current-induced magnetization reversal in nanopillars with perpendicular anisotropy, Nat. Mater. **5**, 210 (2006).

[2] T. Kishi, H. Yoda, T. Kai, T. Nagase, E. Kitagawa, M. Yoshikawa, K. Nishiyama, T. Daibou, M. Nagamine, M. Amano, S. Takahashi, M. Nakayama, N. Shimomura, H. Aikawa, S. Ikegawa, S. Yuasa, K. Yakushiji, H. Kubota, A. Fukushima, M. Oogane, T. Miyazaki, and K. Ando, in *2008 IEEE International Electron Devices Meeting, San Francisco, CA* (IEEE, 2008).

[3] S. Ikeda, K. Miura, H. Yamamoto, K. Mizunuma, H. D. Gan, M. Endo, S. Kanai, J. Hayakawa, F. Matsukura, and H. Ohno, A perpendicular-anisotropy CoFeB-MgO magnetic tunnel junction, Nat. Mater. **9**, 721 (2010).

[4] I. M. Miron, K. Garello, G. Gaudin, P.-J. Zermatten, M. V. Costache, S. Auffret, S. Bandiera, B. Rodmacq, A. Schuhl, and P. Gambardella, Perpendicular switching of a single ferromagnetic layer induced by in-plane current injection, Nature **476**, 189 (2011).

[5] L. Liu, O. J. Lee, T. J. Gudmundsen, D. C. Ralph, and R. A. Buhrman, Current-Induced Switching of Perpendicularly Magnetized Magnetic Layers Using Spin Torque from the Spin Hall Effect, Phys. Rev. Lett. **109**, 096602 (2012).

[6] G. Q. Yu, P. Upadhyaya, Y. B. Fan, J. G. Alzate, W. J. Jiang, K. L. Wong, S. Takei, S. A. Bender, L. T. Chang, Y. Jiang, M. R. Lang, J. S. Tang, Y. Wang, Y. Tserkovnyak, P. K. Amiri, and K. L. Wang, Switching of perpendicular magnetization by spin-orbit torques in the absence of external magnetic fields, Nat. Nanotechnol. **9**, 548 (2014).

[7] H. Yoda, T. Kishi, T. Nagase, M. Yoshikawa, K. Nishiyama, E. Kitagawa, T. Daibou, M. Amano, N. Shimomura, S. Takahashi, T. Kai, M. Nakayama, H. Aikawa, S. Ikegawa, M. Nagamine, J. Ozeki, S. Mizukami, M. Oogane, Y. Ando, S. Yuasa, K. Yakushiji, H. Kubota, Y. Suzuki, Y. Nakatani, T. Miyazaki, and K. Ando, High efficient spin transfer torque writing on perpendicular magnetic tunnel junctions for high density MRAMs, Curr. Appl. Phys. **10**, E87 (2010).

[8] M. Endo, S. Kanai, S. Ikeda, F. Matsukura, and H. Ohno, Electric-field effects on thickness dependent magnetic anisotropy of sputtered $MgO/Co_{40}Fe_{40}B_{20}/Ta$ structures, Appl. Phys. Lett. **96**, 212503 (2010).

[9] K. L. Wang, J. G. Alzate, and P. K. Amiri, Low-power non-volatile spintronic memory: STT-RAM and beyond, J. Phys. D: Appl. Phys. **46**, 074003 (2013).

[10] D. C. Worledge, G. Hu, D. W. Abraham, J. Z. Sun, P. L. Trouilloud, J. Nowak, S. Brown, M. C. Gaidis, E. J. O'Sullivan, and R. P. Robertazzi, Spin torque switching of perpendicular Ta|CoFeB|MgO-based magnetic tunnel junctions, Appl. Phys. Lett. **98**, 022501 (2011).

[11] V. B. Naik, H. Meng, and R. Sbiaa, Thick CoFeB with perpendicular magnetic anisotropy in CoFeB-MgO based magnetic tunnel junction, AIP Adv. **2**, 042182 (2012).

[12] H. Sato, M. Yamanouchi, S. Ikeda, S. Fukami, F. Matsukura, and H. Ohno, Perpendicular-anisotropy CoFeB-MgO magnetic tunnel junctions with a MgO/CoFeB/Ta/CoFeB/MgO recording structure, Appl. Phys. Lett. **101**, 022414 (2012).

[13] H. Sato, E. C. I. Enobio, M. Yamanouchi, S. Ikeda, S. Fukami, S. Kanai, F. Matsukura, and H. Ohno, Properties of magnetic tunnel junctions with a MgO/CoFeB/Ta/CoFeB/MgO recording structure down to junction diameter of 11 nm, Appl. Phys. Lett. **105**, 062403 (2014).

[14] T. Huang, X. Cheng, X. Guan, and X. Miao, Effect of ultrathin inserted Ag layer on perpendicular magnetic anisotropy of CoFeB thin film, IEEE Trans. Magn. **50**, 1 (2014).

[15] L. Cuchet, B. Rodmacq, S. Auffret, R. C. Sousa, I. L. Prejbeanu, and B. Dieny, Perpendicular magnetic tunnel junctions with double barrier and single or synthetic antiferromagnetic storage layer, J. Appl. Phys. **117**, 233901 (2015).

[16] X. Zhang, Y. Zhang, and J. W. Cai, Antiferromagnetically coupled perpendicular magnetic anisotropic CoFeB/MgO films across a Mo spacer with high thermal stability, J. Appl. Phys. **118**, 143903 (2015).

[17] J.-H. Kim, J.-B. Lee, G.-G. An, S.-M. Yang, W.-S. Chung, H.-S. Park, and J.-P. Hong, Ultrathin W space layer-enabled thermal stability enhancement in a perpendicular MgO/CoFeB/W/CoFeB/MgO recording frame, Sci. Rep. **5**, 16903 (2015).

[18] Y. Liu, T. Yu, Z. Y. Zhu, H. C. Zhong, K. M. Khamis, and K. G. Zhu, High thermal stability in W/MgO/CoFeB/W/CoFeB/W stacks via ultrathin W insertion with perpendicular magnetic anisotropy, J. Magn. Magn. Mater. **410**, 123 (2016).

[19] C.-F. Pai, L. Liu, Y. Li, H. W. Tseng, D. C. Ralph, and R. A. Buhrman, Spin transfer torque devices utilizing the giant

spin Hall effect of tungsten, Appl. Phys. Lett. **101**, 122404 (2012).

[20] S. Cho, S. H. C. Baek, K. D. Lee, Y. Jo, and B. G. Park, Large spin Hall magnetoresistance and its correlation to the spin-orbit torque in W/CoFeB/MgO structures, Sci. Rep. **5**, 14668 (2015).

[21] J. Kim, P. Sheng, S. Takahashi, S. Mitani, and M. Hayashi, Spin Hall Magnetoresistance in Metallic Bilayers, Phys. Rev. Lett. **116**, 097201 (2016).

[22] C. He, A. Navabi, Q. Shao, G. Yu, D. Wu, W. Zhu, C. Zheng, X. Li, Q. L. He, S. A. Razavi, K. L. Wong, Z. Zhang, P. K. Amiri, and K. L. Wang, Spin-torque ferromagnetic resonance measurements utilizing spin Hall magnetoresistance in $W/Co_{40}Fe_{40}B_{20}/MgO$ structures, Appl. Phys. Lett. **109**, 202404 (2016).

[23] L. Q. Liu, T. Moriyama, D. C. Ralph, and R. A. Buhrman, Spin-Torque Ferromagnetic Resonance Induced by the Spin Hall Effect, Phys. Rev. Lett. **106**, 036601 (2011).

[24] A. R. Mellnik, J. S. Lee, A. Richardella, J. L. Grab, P. J. Mintun, M. H. Fischer, A. Vaezi, A. Manchon, E. A. Kim, N. Samarth, and D. C. Ralph, Spin-transfer torque generated by a topological insulator, Nature **511**, 449 (2014).

[25] T. X. Nan, S. Emori, C. T. Boone, X. J. Wang, T. M. Oxholm, J. G. Jones, B. M. Howe, G. J. Brown, and N. X. Sun, Comparison of spin-orbit torques and spin pumping across NiFe/Pt and NiFe/Cu/Pt interfaces, Phys. Rev. B **91**, 214416 (2015).

[26] S. Mizukami, Y. Ando, and T. Miyazaki, The study on ferromagnetic resonance linewidth for NM/80NiFe/NM (NM = Cu, Ta, Pd andPt) films, Japan, J. Appl. Phys. **40**, 580 (2001).

[27] T. Kensho, M. Takahiro, N. Masaki, S. Takeshi, T. Koki, T. Saburo, and O. Teruo, Linewidth broadening of optical precession mode in synthetic antiferromagnet, Appl. Phys. Express **7**, 063010 (2014).

[28] M. Belmeguenai, T. Martin, G. Woltersdorf, M. Maier, and G. Bayreuther, Frequency- and time-domain investigation of the dynamic properties of interlayer-exchange-coupled $Ni_{81}Fe_{19}/Ru/Ni_{81}Fe_{19}$ thin films, Phys. Rev. B **76**, 104414 (2007).

[29] H. Yang, Y. Li, and W. E. Bailey, Large spin pumping effect in antisymmetric precession of $Ni_{79}Fe_{21}/Ru/Ni_{79}Fe_{21}$, Appl. Phys. Lett. **108**, 242404 (2016).

[30] B. Heinrich, J. F. Cochran, M. Kowalewski, J. Kirschner, Z. Celinski, A. S. Arrott, and K. Myrtle, Magnetic anisotropies and exchange coupling in ultrathin fcc Co(001) structures, Phys. Rev. B **44**, 9348 (1991).

[31] S. Takahashi, Giant enhancement of spin pumping in the out-of-phase precession mode, Appl. Phys. Lett. **104**, 052407 (2014).

[32] N. Wiese, T. Dimopoulos, M. Ruhrig, J. Wecker, H. Bruckl, and G. Reiss, Antiferromagnetically coupled CoFeB/Ru/CoFeB trilayers, Appl. Phys. Lett. **85**, 2020 (2004).

[33] J.-B. Lee, G.-G. An, S.-M. Yang, H.-S. Park, W.-S. Chung, and J.-P. Hong, Thermally robust perpendicular Co/Pd-based synthetic antiferromagnetic coupling enabled by a W capping or buffer layer, Sci. Rep. **6**, 21324 (2016).

[34] M. A. Ruderman and C. Kittel, Indirect exchange coupling of nuclear magnetic moments by conduction electrons, Phys. Rev. **96**, 99 (1954).

[35] T. Kasuya, A theory of metallic ferromagnetism and antiferromagnetism on Zeners model, Prog. Theor. Phys. **16**, 45 (1956).

[36] K. Yosida, Magnetic properties of Cu-Mn alloys, Phys. Rev. **106**, 893 (1957).

[37] P. Bruno and C. Chappert, Oscillatory Coupling between Ferromagnetic Layers Separated by a Nonmagnetic Metal Spacer, Phys. Rev. Lett. **67**, 1602 (1991).

[38] P. Bruno and C. Chappert, Ruderman-Kittel theory of oscillatory interlayer exchange coupling, Phys. Rev. B **46**, 261 (1992).

[39] J. Moritz, F. Garcia, J. C. Toussaint, B. Dieny, and J. P. Nozieres, Orange peel coupling in multilayers with perpendicular magnetic anisotropy: Application to (Co/Pt)-based exchange-biased spin-valves, Europhys. Lett. **65**, 123 (2004).

[40] A. Layadi and J. O. Artman, Ferromagnetic resonance in a coupled two-layer system, J. Magn. Magn. Mater. **92**, 143 (1990).